J Mater Sci (2006) 41:6673–6692
DOI 10.1007/s10853-006-0204-7

Multi-scale dynamic failure prediction tool for marine composite structures

James Lua · William Gregory · Jagannathan Sankar

Published online: 8 August 2006

Abstract A high fidelity assessment of accumulative damage of woven fabric composite structures subjected to aggressive loadings is strongly reliant on the accurate characterization of the inherent multi-scale microstructures and the underlying deformation phenomena. Damage in composite sandwich and joint structures is characterized by the coexistence of discrete (delamination) and continuum damage (matrix cracking and intralaminar damage). A purely fracture mechanics-based or a purely continuum damage mechanics-based tool alone cannot effectively characterize the interaction between the discrete and continuum damage and their compounding effect that leads to the final rupture. In this paper, a hybrid discrete and continuum damage model is developed and numerically implemented within the LS-DYNA environment via a user-defined material model. The continuum damage progression and its associated stiffness degradation are predicted based on the constituent stress/strain and their associated failure criteria while the discrete delamination damage is captured via a cohesive interface model. A multi-scale computational framework is established to bridge the response and failure predictions at constituent, ply, and laminated composite level. The calculated constituent stress and strain are used in a mechanism-driven failure criterion to predict the failure mode, failure sequence, and the synergistic interaction that leads to global stiffness degradation and the final rupture. The use of the cohesive interface model can capture the complicated delamination zone without posing the self-similar crack growth condition. The unified depiction of the continuum and discrete damage via the damage mechanics theory provides a rational way to study the coupling effects between the in-plane and the out-of-plane failure modes. The applicability and accuracy of the damage models used in the hybrid dynamic failure prediction tool are demonstrated via its application to a circular plate and a composite hat stiffener subjected to shock and low velocity impact loading. The synergistic interaction between the continuum and discrete damage is explored via its application to a sandwich beam subjected to a low velocity impact.

J. Lua (✉)
Applied Mechanics Department, Anteon Corporation, SEG/Engineering Technology Center, 240 Oral School Road, Suite 105, Mystic, CT 06355-1208, USA
e-mail: jlua@anteon.com

W. Gregory
Anteon Corporation, SEG/Engineering Technology Center, 1100 New Jersey Avenue, SE Suite 200, Washington, DC 20003, USA

J. Sankar
Center for Advanced Materials and Smart Structures, NC A&T State University, 1601 E. Market Street, Greensboro, NC 27411, USA

Introduction

Fiber-reinforced polymer (FRP) composites have been increasingly used in the current and next generation of naval ships (e.g., composite hull, composite topside, composite mast, composite sail, hybrid hull, etc.). The most compelling reasons to use composite materials in naval ship components are stealth, lower total ownership cost, and weight reduction. The composite materials have played key roles in reducing the magnetic, acoustic, hydrodynamic, radar, and thermal signatures and increasing payload, top speed, and operation range. Current composite structural design requires time-consuming and expensive sub-component and full-scale component testing to

establish damage tolerance certification, resulting in the investment of a significant amount of resources in the material/structure certification phase. Given the time and budget constraints, the development of a prediction tool for damage onset and/or growth in composite structures can play a key role in determining the design allowables, which are often the limiting factor for structural efficiency and load-carrying capacity.

Naval ship structures are subjected to low/high velocity impact-induced damage during their service life caused by ice impact, grounding, dropping tools during maintenance operations, high impulsive shock waves from weapon effects, etc. The fact that some of these impact events may take place without leaving any visible evidence on the surface of an impacted laminate makes it even more important to account for these loading cases in the design process. The non-inspectable and hidden damage resulting from the dynamic impact has posed a great challenge in designing and maintaining the damage tolerant composite ship structures. The use of a ''knock-down'' factor based on limited number of impact tests will result in a design of unknown risk. The added unnecessary weight will have a big impact on the payload, top speed, and operation range of a ship. The development of a reliable impact damage assessment tool is extremely important in decision making regarding the continue operation or deport repair and maintenance action after an impact accident. Using the numerical simulation tool, a cost-effective design procedure can be implemented by replacing the test-driven certification process with performance-driven design iterations.

Woven fabric composites have unique tailoring capabilities for improving the impact resistance and high strength of naval ship structural components. However, the complex architecture of woven fabric composites makes response and failure prediction very difficult and computationally intensive. Both in-plane damage resulted from the shear cracking, matrix cracking, or the fiber breakage, and out-of-plane damage induced by delamination coexist and their synergistic interactions to the final failure depend on the constituent materials, woven fabric micro-structural parameters, stacking sequence, and geometric and loading configurations. As stated by Yang and Cox [1] recently, failure analysis involving both in-plane failure modes and interlaminar delamination are far fewer, mainly due to the complex nature of the coupling between in-plane and out-of-plane damage events.

The continuum damage mechanics approach has been used extensively in characterizing the in-plane damage as shown in Refs. [2–6]. Most of the current continuum damage mechanics approaches apply the composite-level stress and strain in a failure criterion to predict the stiffness degradation. However, it is the constituent stress and strain that drive the constituent failure and the resulting stiffness degradation at the composite level. Recognized that the energy dissipates by various damage or fracturing processes at constituent levels, the use of constitutive stress and strain in a mechanism driven failure criterion has become the recent subject of many research works [7–11].

The propagation of discrete damage in a form such as a delamination or a debonding crack has been studied extensively using either the cohesive interface element [12, 13] or the virtual crack closure technique (VCCT) [14, 15]. Since VCCT is primarily based on the theory of linear elastic fracture mechanics (LEFM), it is only applicable for a Griffith crack that grows in a self-similar manner. While a Griffith crack can exist initially in a composite structure, mechanisms such as fiber bridging across the crack surface, interfacial fractional effect, non-linear crack tip crazing zone, and delamination kinking may render the LEFM-based VCCT inapplicable. In addition, an initial guess in delamination size and location has to be pre-defined in VCCT which will preclude its solution for solving free edge crack nucleation and propagation, and delamination in a composite panel due to low-velocity impact. On the contrary, the damaged mechanics based cohesive interface element can characterize both the brittle and ductile fracture without posing the self-similar crack propagation. The cohesive law, which relates the traction across the interface to its separation, can capture the friction contact and bridging due to the present of resin fragments, surface roughness, and the through-thickness reinforcement. With the aid of the cohesive interface element, the discrete delamination damage can be captured using the continuum damage mechanics approach. Thus, a unified depiction of the continuum and discrete damage can be achieved based on the damage mechanics theory to quantify the synergistic interaction between the diffuse in-plane damage and the discrete out-of-plane delamination.

The coupling effects between the diffuse in-plane damage and discrete out-of-plane delamination have not been adequately addressed to date [1]. The stiffness degradation from the continuum in-plane damage will have a direct impact on the inter-laminar stress and the resulting delamination initiation and propagation. In addition, the intensified stress field in the vicinity of a moving crack tip will initiate new micro-damage that will accelerate the stiffness degradation. Therefore, to accurately characterize the damage progression in composite structures, the embedded constitutive models of a FEM solver have to capture both discrete and continuous damage along with their interactions.

An accurate assessment of the accumulative damage to a composite ship structure subjected to an aggressive loading environment strongly relies on the accurate characterization of the inherent multi-scale microstructures and the

underlying deformation phenomena. The stress and strain fields predicted at a global structural level are unable to determine the damage and failure mechanisms at the constituent level and the resulting stiffness degradation. To capture the synergistic interaction of constituent failure modes that leads to material degradation and final rupture, the stress/strain response at each microstructural level has to be determined from given macro stress/strain response parameters. Given the constituent stress and strain and the associated mechanism-driven failure criteria, the material degradation at each constituent can be quantified. Finally, to propagate the damage from the constituent to the structural level, a multilevel homogenization has to be performed. Therefore, to implement a multi-scale progressive failure analysis, a dual-function micromechanics model has to be developed to (1) decompose the response parameters from the global structural level to microstructural levels for the failure mode prediction and (2) homogenize damaged material properties at the global structural level based on the damaged material properties at microstructural levels for the damage prediction at the next loading stage. As both the decomposition and homogenization procedures have to be performed at each Gaussian point and at each time step during a finite-element-based dynamic progressive failure analysis, it is imperative to develop an efficient micromechanics model while retaining sufficient accuracy.

In this study, a hybrid discrete and continuum damage model is developed and numerically implemented within the LS-DYNA environment via a user-defined material model. The delamination failure along an interface is characterized by the cohesive element approach with a user-defined cohesive law. The in-plane damage resulting from the fiber/tow/matrix failure in a woven fabric composite is characterized using a continuum damage model. To capture the mechanism driven stiffness degradation, the constituent stress and strain are computed first from the composite-level stress/strain using the recently developed micromechanics tool, CELLMAT. The CELLMAT tool serves as a dual-function micromechanics model to (1) quantify the thermal–mechanical composite material properties of an unbalanced weave at a given constituent damage state and (2) establish the mapping relation of the stress/strain response between the microstructural and macrostructural levels. A logical diagram along with the key solution components of the dynamic failure prediction tool is shown in Fig. 1. As can be seen from Fig. 1, a multi-scale framework has been established to bridge the response and damage prediction at the constituent, ply, laminated plate, and composite structure level.

An overview of the CELLMAT solver is described first followed by a brief description of the mechanism driven failure criteria. A bridging model is formed to quantify laminate response from a given damaged ply distribution. After establishing the multi-scale framework for characterizing the continuum damage, a cohesive interface model is presented along with its numerical implementation. By integrating the multi-scale continuum damage model with the cohesive interface model, a hybrid dynamic failure prediction tool is given along with a summary of the numerical solution procedure. Three example applications of the hybrid dynamic failure prediction tool are introduced to demonstrate its applicability and solution accuracy: (1) a circular laminate plate subjected to a dynamic shock

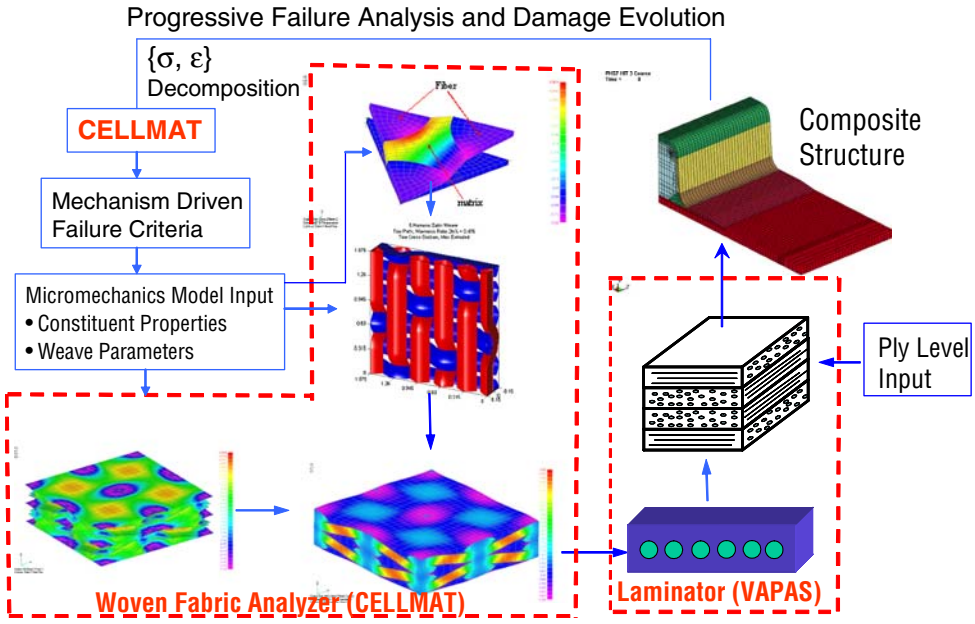

Fig. 1 An overview of multi-scale response characterization and failure prediction of composite structures

loading; (2) a composite hat stiffener subjected to a low velocity impact on the bottom baseplate; and (3) a sandwich beam subjected to a drop weight impact.

Micromechanics cell model for an unbalanced plain weave

In order to accurately capture the diffuse in-plane damage and the resulting stiffness degradation, a four-cell micromechanics model is developed to quantify the constituent damage induced ply properties and decompose the stress and strain from the composite level to its constituent level for the constituent based failure prediction. The finite element based micromechanics model (TMAT) has been developed for the thermal–mechanical response prediction of a balanced weave [16–18]. Despite the automatic FEM solution process used in TMAT, it is not well-suited for the dynamic progressive failure prediction of a large composite structure. This is because the TMAT solver needs to be executed for each Gaussian point and at each time step. To circumvent this difficulty, a set of discrete damage states are pre-defined based on the failure logic in Ref. [11] where material properties at each of these damages states are computed in advance using the micromechanics model. However, the replacement of a continuous damage space by a set of discrete ones cannot capture various failure scenarios associated with combined loading cases. In addition, the lack of continuous stiffness degradation among these damage states may introduce spurious numerical noise in time dependent stress/strain response predictions.

Because of the high computational cost associated with a finite-element-based micromechanics model and limitations of an oversimplified micromechanics model in accurately capturing the microstructures and the underlying deformation phenomena, a four-cell micromechanics model [19] is selected for its implementation in the hybrid damage prediction tool to enhance the numerical efficiency while retaining sufficient accuracy for constituent response prediction. Since the commonly used naval composites are unbalanced plain weave with the warp tows spaced 5.1 mm (5 tows per inch) and fill tows spaced at 6.4 mm (4 tows per inch) as shown in Fig. 2, the original four-cell method [20] for a balanced weave has been extended in Ref. [19] for the thermal–mechanical response prediction of an unbalanced weave.

The cell-based micromechanics model is developed based on a multi-constituent homogenization in conjunction with the iso-stress and iso-stress description. The representative volume element (RVE) of an unbalanced weave is first decomposed to its subcells and the multi-constituent homogenization is then applied for each subcell to establish the mapping relation between the subcell and its constituent response parameters. After homogenizing each subcell, a parallel-series approach is then applied to determine the thermal mechanical response of the RVE from the response parameters of each of its subcells.

The cell decomposition procedure is illustrated here using the TMAT micromechanics model of a balanced weave. As shown in Fig. 3, the RVE is first simplified by using quarter-symmetry. Next, the 1/4th RVE is further decomposed into the XY-, XR-, YR-, and RR- cells. The

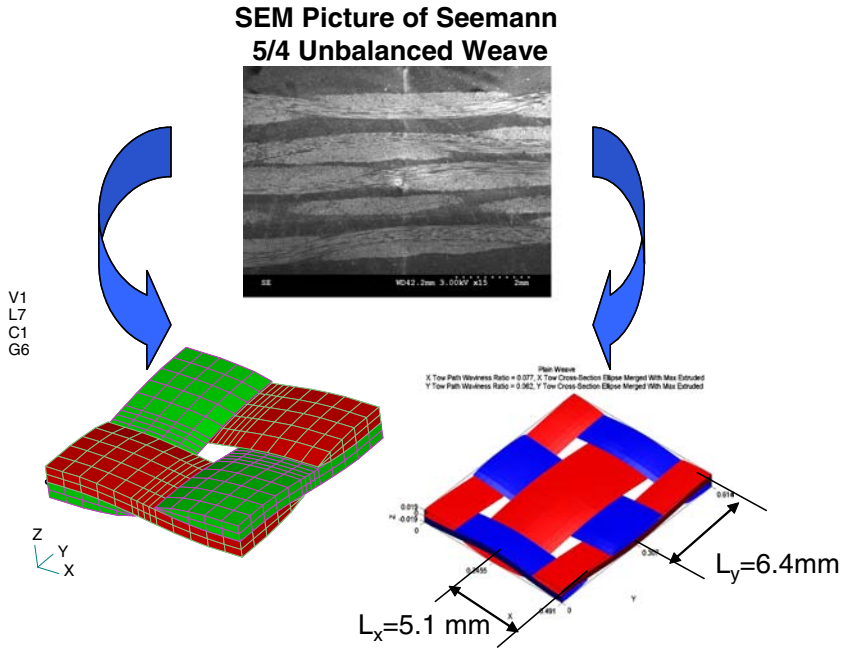

Fig. 2 Comparison of balanced and unbalanced weave representation of a Seemann composite system

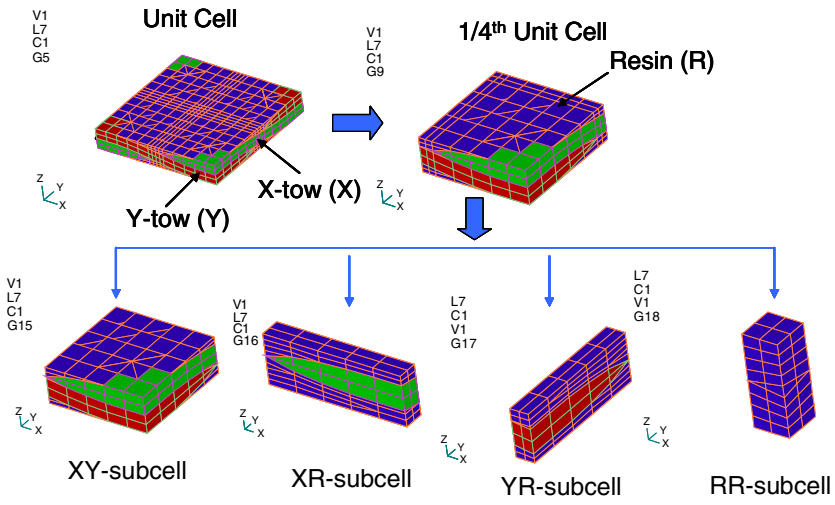

Fig. 3 Illustration of basic steps in cell decomposition

XY-cell consists of primarily the X- and Y-tow with a small volume fraction in resin (R). In XR- and YR- cells, the tow (X or Y) volume fraction and the resin volume fraction (R) is assumed the same. For the RR-cell, 100% of the material is resin (resin pocket). These four individual cells form the basic building blocks of the 1/4th unit cell model.

To characterize each of these four basic building blocks by the cell homogenization model, two simplifications are used as follows: (1) the tow cross-sectional shape is assumed to be rectangular; and (2) the undulated X- and Y-tow is replaced with a straight line segment. The resulting simplified four-cell representation of the unbalanced weave is depicted in Fig. 4. Four microstructural parameters are used to characterize the weave architecture: (1) tow thickness (H_{tow}); (2) tow volume fraction within the 1/4th unit cell (V_{tow}); (3) the X-tow spacing (L_y); and (4) the Y-tow spacing (L_x). The size of the 1/4th unit cell in dimensionless space is defined by $\bar{L}_y = L_y/L_y = 1.0, \bar{L}_x = L_x/L_y$, and $\bar{H} = H/L_y$. Using these dimensionless parameters, the length of the straight portion of either the X- or Y-tow (V_f), the X-tow angle (θ_x) in the XR-subcell, and the Y-tow angle (θ_y) in the YR-subcell can be determined by

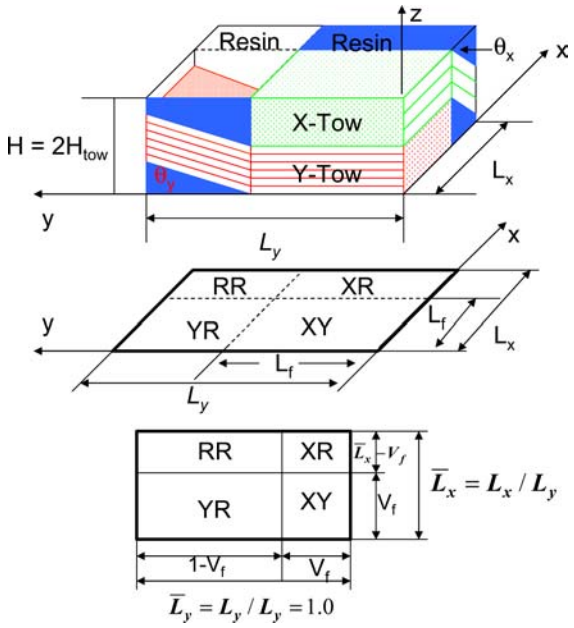

Fig. 4 Four-cell representation of an unbalanced plain weave

$$V_f = 2\bar{L}_x V_{\text{tow}}/(1+\bar{L}_x) \tag{1}$$

$$\theta_x = \tan^{-1}\left[\bar{H}/4(\bar{L}_x - V_f)\right] \tag{2}$$

$$\theta_y = \tan^{-1}\left[\bar{H}/4(1 - V_f)\right] \tag{3}$$

Given the overall fiber volume fraction in RVE of V_f^{RVE}, the fiber volume fraction within a tow can be calculated by

$$V_f^{\text{tow}} = \frac{2V_f^{\text{RVE}}\bar{L}_x}{V_f(1+\bar{L}_x)} \tag{4}$$

For a balanced weave, we have $\bar{L}_x = L_x/L_y = 1.0$. Using Eqs. (1) and (4), we have $V_f = V_{\text{tow}}$ and $V_f^{\text{tow}} = V_f^{\text{RVE}}/V_f$. As can be seen from Fig. 4, except for the RR-cell, each cell consists of two material phases. The complete derivation of the thermal–mechanical decomposition model for each subcell can be found in Ref. [19]. For illustration purpose, the derivation of the thermal–mechanical decomposition model for the XY-subcell is summarized below.

As shown in Fig. 4, the XY-cell is filled completely with the straight part of the X-tow and Y-tow with the same subcell volume fraction. Unlike the balanced weave, a

distinct thermal–mechanical constitutive model is used to characterize both the X- and the Y-tow. For the XY-cell, it is assumed that the global unit cell coordinate system shown in Fig. 4 coincides with the XY-cell coordinate system. Given the orthotropic behavior of the X-tow and Y-tow defined in the material coordinate system, the constituent behavior of the X- and Y-tow in the XY-cell coordinate system is defined by

$$\begin{Bmatrix} \sigma^X_{xx} \\ \sigma^X_{yy} \\ \sigma^X_{zz} \\ \sigma^X_{yz} \\ \sigma^X_{zx} \\ \sigma^X_{xy} \end{Bmatrix} = \begin{bmatrix} C^X_{11} & C^X_{12} & C^X_{12} & 0 & 0 & 0 \\ C^X_{12} & C^X_{22} & C^X_{23} & 0 & 0 & 0 \\ C^X_{12} & C^X_{23} & C^X_{22} & 0 & 0 & 0 \\ 0 & 0 & 0 & C^X_{44} & 0 & 0 \\ 0 & 0 & 0 & 0 & C^X_{55} & 0 \\ 0 & 0 & 0 & 0 & 0 & C^X_{55} \end{bmatrix} \begin{Bmatrix} \varepsilon^X_{xx} - \alpha^X_1 \Delta T \\ \varepsilon^X_{yy} - \alpha^X_2 \Delta T \\ \varepsilon^X_{zz} - \alpha^X_3 \Delta T \\ \gamma^X_{yz} \\ \gamma^X_{zx} \\ \gamma^X_{xy} \end{Bmatrix} \tag{5}$$

$$\begin{Bmatrix} \sigma^Y_{xx} \\ \sigma^Y_{yy} \\ \sigma^Y_{zz} \\ \sigma^Y_{yz} \\ \sigma^Y_{zx} \\ \sigma^Y_{xy} \end{Bmatrix} = \begin{bmatrix} C^Y_{22} & C^Y_{12} & C^Y_{23} & 0 & 0 & 0 \\ C^Y_{12} & C^Y_{11} & C^Y_{12} & 0 & 0 & 0 \\ C^Y_{23} & C^Y_{12} & C^Y_{22} & 0 & 0 & 0 \\ 0 & 0 & 0 & C^Y_{55} & 0 & 0 \\ 0 & 0 & 0 & 0 & C^Y_{44} & 0 \\ 0 & 0 & 0 & 0 & 0 & C^Y_{55} \end{bmatrix} \begin{Bmatrix} \varepsilon^Y_{xx} - \alpha^Y_2 \Delta T \\ \varepsilon^Y_{yy} - \alpha^Y_1 \Delta T \\ \varepsilon^Y_{zz} - \alpha^Y_3 \Delta T \\ \gamma^Y_{yz} \\ \gamma^Y_{zx} \\ \gamma^Y_{xy} \end{Bmatrix} \tag{6}$$

where the superscript X and Y in Eqs. (5) and (6) denote the parameter associated with the X-tow and Y-tow, respectively, and the subscript 1, 2, and 3 given in the stiffness matrix [**C**] and the coefficient of thermal expansion vector $\{\boldsymbol{\alpha}\}$ represent the property variable defined along the tow (1) and transverse to the tow (2, 3) direction. Given the perfect bonding of X- and Y-tow within the XY-subcell, the iso-strain $\{\varepsilon^{XY}_{xx}, \varepsilon^{XY}_{yy}, \gamma^{XY}_{xy}\}$ and the iso-stress $\{\sigma^{XY}_{zz}, \sigma^{XY}_{yz}, \sigma^{XY}_{zx}\}$ of the XY-subcell are assumed to be the same as the corresponding stress and strain in the X- and Y-tow, namely,

$$\begin{aligned} \varepsilon^X_{xx} &= \varepsilon^Y_{xx} = \varepsilon^{XY}_{xx}, \quad & \sigma^X_{zz} &= \sigma^Y_{zz} = \sigma^{XY}_{zz} \\ \varepsilon^X_{yy} &= \varepsilon^Y_{yy} = \varepsilon^{XY}_{yy}, \quad & \sigma^X_{yz} &= \sigma^Y_{yz} = \sigma^{XY}_{yz} \\ \gamma^X_{xy} &= \gamma^Y_{xy} = \gamma^{XY}_{xy}, \quad & \sigma^X_{zx} &= \sigma^Y_{zx} = \sigma^{XY}_{zx} \end{aligned} \tag{7}$$

Rearranging the strain and stress in Eqs. (5) and (6) in terms of iso-strain $\{\boldsymbol{\varepsilon}_n = \{\boldsymbol{\varepsilon}_{xx}, \boldsymbol{\varepsilon}_{yy}, \boldsymbol{\gamma}_{xy}\}$ and iso-stress $\{\boldsymbol{\sigma}_s\} = \{\boldsymbol{\sigma}_{zz}, \boldsymbol{\sigma}_{yz}, \boldsymbol{\sigma}_{zx})$, Eqs. (5) and (6) can be rewritten as

$$\begin{Bmatrix} \sigma^k_n \\ \sigma^k_s \end{Bmatrix} = \begin{Bmatrix} \sigma^k_{xx} \\ \sigma^k_{yy} \\ \sigma^k_{xy} \\ \sigma^k_{zz} \\ \sigma^k_{yz} \\ \sigma^k_{zx} \end{Bmatrix} = \begin{bmatrix} C^k_{nn} & C^k_{ns} \\ C^k_{sn} & C^k_{ss} \end{bmatrix} \begin{Bmatrix} \varepsilon^k_n \\ \varepsilon^k_s \end{Bmatrix} + \begin{Bmatrix} \sigma^k_{Tn} \\ \sigma^k_{Ts} \end{Bmatrix} \tag{8}$$

where k is an index representing either X or Y and the thermal stress vector $\{\sigma^k_{Tn}\}$ and $\{\sigma^k_{Ts}\}$ in Eq. (8) is define by $\{\sigma^k_{Tn}\}=\{\sigma^k_{Txx},\sigma^k_{Tyy},\sigma^k_{Txy}\}'$ and $\{\sigma^k_{sn}\}=\{\sigma^k_{Tzz},\sigma^k_{Tyz},\sigma^k_{Tzx}\}'$, respectively. The four stiffness matrices (C^k_{nn} ,C^k_{ns},C^k_{sn},C^k_{ss}) in Eq. (8) can be determined from the partitioning the effective stiffness matrix defined in Eq. (5) or Eq. (6) using the iso-strain ($\boldsymbol{\varepsilon}_n$) and the iso-stress ($\boldsymbol{\sigma}_s$) definition. The thermal stress $\{\sigma^k_{Tn},\sigma^k_{Ts}\}$ can be computed from the thermal strain by

$$\sigma^k_{Tn} = -\left[C^k_{nn}\varepsilon^k_{Tn} + C^k_{ns}\varepsilon^k_{Ts}\right]; \text{ and } \sigma^k_{Ts} = -\left[C^k_{sn}\varepsilon^k_{Tn} + C^k_{ss}\varepsilon^k_{Ts}\right] \tag{9}$$

For a general orthotropic material subjected to a given temperature jump ΔT, the thermal strain for the kth constituent can be computed by

$$\begin{Bmatrix} \varepsilon^k_{Tn} \\ \varepsilon^k_{Ts} \end{Bmatrix} = \begin{Bmatrix} \varepsilon^k_{Txx} \\ \varepsilon^k_{Tyy} \\ \gamma^k_{Txy} \\ \varepsilon^k_{Tzz} \\ \gamma^k_{Tyz} \\ \gamma^k_{Tzx} \end{Bmatrix} = \begin{bmatrix} \alpha^k_x \\ \alpha^k_y \\ 0 \\ \alpha^k_z \\ 0 \\ 0 \end{bmatrix} \Delta T \tag{10}$$

Substituting Eq. (7) into Eq. (8), the unknown constituent stress and strain can be determined from a given iso-stress $\{\sigma^{XY}_s\}$ and strain $\{\varepsilon^{XY}_n\}$ of the XY-subcell by

$$\begin{aligned} \left\{\sigma^k_n\right\} =& \left[\left[C^k_{nn}\right] - \left[C^k_{ns}\right]\left[C^k_{ss}\right]^{-1}\left[C^k_{sn}\right]\right]\left\{\varepsilon^{XY}_n\right\} \\ &+ \left[C^k_{ns}\right]\left[C^k_{ss}\right]^{-1}\left\{\sigma^{XY}_s\right\} \\ &+ \left[\left[C^k_{ns}\right]\left[C^k_{ss}\right]^{-1}\left[C^k_{sn}\right] - \left[C^k_{nn}\right]\right]\varepsilon^k_{Tn}; \quad k = X, Y \end{aligned} \tag{11}$$

$$\left\{\varepsilon_s^k\right\} = \left[C_{ss}^k\right]^{-1}\left[\left\{\sigma_s^{XY}\right\} - \left[C_{sn}^k\right]\left[\left\{\varepsilon_n^{XY}\right\} - \left\{\varepsilon_{Tn}^k\right\}\right]\right] + \left\{\varepsilon_{Ts}^k\right\}; \quad k = X, Y \tag{12}$$

Using Eqs. (7), (11), and (12), all the stress and strain in either X- or Y-tow can be solved from the stress and strain defined in subcell XY ($\boldsymbol{\sigma}^{\mathrm{XY}}, \boldsymbol{\varepsilon}^{\mathrm{XY}}$). Thus, a stress and strain decomposition module is formed for the XY-subcell where the constituent stress and strain can be determined from the stress and strain at the subcell level.

The decomposition module for the remaining subcells (XR, YR, RR) can be derived in exactly the same way as for the XY-subcell. Next, the mapping relations between the subcell stress/strain $\{\boldsymbol{\sigma}^{\mathrm{SC}}, \boldsymbol{\varepsilon}^{\mathrm{SC}}; \mathrm{SC} = \mathrm{XY}, \mathrm{XR}, \mathrm{YR}, \mathrm{RR}\}$ and the global unit cell stress/strain $\{\boldsymbol{\sigma}^{\mathrm{RVC}}, \boldsymbol{\varepsilon}^{\mathrm{RVC}}\}$ are developed using a parallel-series approach described by Ivanov and Tabiei [20]. With the aid of this two-level decomposition, the subcell stress/strain $\{\boldsymbol{\sigma}^{\mathrm{SC}}, \boldsymbol{\varepsilon}^{\mathrm{SC}}\}$ are computed first from the global unit cell stress/strain $\{\boldsymbol{\sigma}^{\mathrm{RVC}}, \boldsymbol{\varepsilon}^{\mathrm{RVC}}\}$ followed by the determination of the constituent stress/strain $\{\boldsymbol{\sigma}^k, \boldsymbol{\varepsilon}^k; k = X, Y, R\}$ from the subcell stress and strain $\{\boldsymbol{\sigma}^{\mathrm{SC}}, \boldsymbol{\varepsilon}^{\mathrm{SC}}\}$.

The nine (9) equivalent elastic constants (E_1, E_2, E_3, G_{12}, G_{23}, G_{31}, ν_{21}, ν_{31}, ν_{32}) of a ply (RVE) are determined by applying the energy equivalence of the RVE subjected to 9 independent global strain fields. These nine uniform strain fields of the RVE are associated with the non-zero tensile strain in *x*-, *y*-, and *z*- direction, non-zero shear in *xy*-, *yz*-, and *zx*-plane, and the biaxial strain in *x*/*y*-, *y*/*z*-, and *z*/*x*-direction. After determining the equivalent material properties of the ply [**C**], the three equivalent coefficient of thermal expansion $\{\alpha_1, \alpha_2, \alpha_3\}$ of the ply is computed from the thermal–mechanical cell model by

$$\begin{bmatrix} C_{11} & C_{12} & C_{13} \\ C_{12} & C_{22} & C_{23} \\ C_{13} & C_{23} & C_{33} \end{bmatrix} \begin{Bmatrix} \alpha_1 \\ \alpha_2 \\ \alpha_3 \end{Bmatrix} = - \begin{Bmatrix} \sigma_{11}^T \\ \sigma_{22}^T \\ \sigma_{33}^T \end{Bmatrix} \tag{13}$$

where σ_{11}^T,σ_{22}^T, and σ_{33}^T are the components of the residual thermal stress of RVE associated with a unit temperature increase subjected to a zero-displacement constraint ($u_x = u_y = u_z = 0.0$) in RVE.

The four-cell representation of an unbalanced plain weave unit cell provides a hierarchical micromechanics framework for quantification of constituent damage induced thermal–mechanical properties and stress/strain response at multi-scale levels. A dual-function micromechanics model, CELLMAT, based on the above cell method, is developed for an unbalanced weave subjected to a thermal–mechanical load. The woven fabric analyzer in CELLMAT serves as a material virtual testing tool to determine the effective thermal–mechanical properties at the composite level for given microstructural and constituent material parameters. The two-level stress/strain decomposition in CELLMAT establishes a link among the response parameters at different microstructural levels. Because of the high computational efficiency, CELLMAT is ideally suited for its use in the finite-element-based failure prediction where the degraded thermal–mechanical properties have to be determined at each Gaussian point and at each time step.

Mechanism-driven failure criteria and continuum damage progression

Most of composite failure criteria are derived for a unidirectional composite. Advanced failure criteria exist that distinguish modes of failure, for instance, compressive matrix failure, tensile matrix failure, compressive fiber failure, and tensile fiber failure. Hashin's criteria [21] were the first to make this distinction. While not as popular among analysts as the simpler, tensorial and Tsai envelop criteria [22], Hashin's criteria, and its derivatives, are used by most researchers [23].

Due to the lack of mechanism based failure criteria for woven fabric composites, existing failure criteria of a unidirectional composite have been modified for the damage and failure prediction of a woven fabric composite. The physical basis behind this is that each tow in the woven fabric composite can be characterized as a unidirectional composite. This approach is valid if the stress/strain of a tow is used in the failure criteria of the unidirectional composite. However, many researchers have used the composite level $\boldsymbol{\sigma}/\boldsymbol{\varepsilon}$ as the tow $\boldsymbol{\sigma}/\boldsymbol{\varepsilon}$ in the failure criteria derived from the unidirectional composites.

In this study, the stress and strain in each of these three (3) constituents (X-tow/Y-tow/resin) are determined from the $\boldsymbol{\sigma}/\boldsymbol{\varepsilon}$ at the composite level using CELLMAT. Given the $\boldsymbol{\sigma}/\boldsymbol{\varepsilon}$ defined in the local material coordinate of a tow and resin, modified Hashin's criteria listed in Table 1 are used for each constituent. Two types of failure criteria are employed to distinguish the tensile failure mode from the compressive failure mode. Given the unit-cell coordinate system defined in Fig. 4, the stress along the X-tow is σ_1 while the stress along the Y-tow is σ_2. Note that the σ_1 used in the X-tow tensile failure criterion and σ_2 in the Y-tow tensile failure criterion are the average tow-stress along the X-tow, and Y-tow, respectively. Based on this notation, the other constituent stress components defined in the constituent failure criteria are self-explanatory. In Table 1, the constituent strength parameters are defined by

X_{T}, Y_{T}, and Z_{T}—Axial and transverse tensile strength of a tow

Table 1 Summary of mechanism-driven failure criteria in each constituent

Constituent failure modes	Tensile failure	Compressive failure
X-tow (along the fiber direction)	$\left(\frac{\sigma_1}{X_T}\right)^2+\left(\frac{\tau_{12}+\tau_{13}}{T_L}\right)^2\geq 1;\quad \sigma_1>0$	$\left(\frac{\sigma_1}{X_C}\right)^2\geq 1;\quad \sigma_1<0$
X-tow (perpendicular to the fiber direction)	$\left(\frac{\sigma_2}{Y_T}\right)^2+\left(\frac{\tau_{21}+\tau_{23}}{T_T}\right)^2\geq 1;\quad \sigma_2>0$	$\frac{\sigma_2}{Y_C}\left[\left(\frac{Y_C}{2T_T}\right)^2-1\right]+\left(\frac{\sigma_2}{2T_T}\right)^2+\left(\frac{\tau_{21}}{T_L}\right)^2\geq 1;\quad \sigma_2<0$
Y-tow (along the fiber direction)	$\left(\frac{\sigma_2}{X_T}\right)^2+\left(\frac{\tau_{21}+\tau_{23}}{T_L}\right)^2\geq 1;\quad \sigma_2>0$	$\left(\frac{\sigma_2}{X_C}\right)^2\geq 1;\quad \sigma_2<0$
Y-tow (perpendicular to the fiber direction)	$\left(\frac{\sigma_1}{Y_T}\right)^2+\left(\frac{\tau_{12}+\tau_{13}}{T_T}\right)^2\geq 1;\quad \sigma_1>0$	$\frac{\sigma_1}{Y_C}\left[\left(\frac{Y_C}{2T_T}\right)^2-1\right]+\left(\frac{\sigma_1}{2T_T}\right)^2+\left(\frac{\tau_{12}}{T_L}\right)^2\geq 1;\sigma_1<0$
Delamination failure	$\left(\frac{\sigma_{33}}{Z_T}\right)^2+\left(\frac{\tau_{13}}{T_L}\right)^2+\left(\frac{\tau_{23}}{T_T}\right)^2\geq 1;\quad \sigma_3>0$	$\frac{\sigma_3}{Z_C}\left[\left(\frac{Z_C}{2T_L}\right)^2-1\right]+\left(\frac{\tau_{13}}{T_L}\right)^2+\left(\frac{\tau_{23}}{T_T}\right)^2\geq 1;\quad \sigma_3<0$
In-plane matrix shear failure (resin)	$\left(\frac{\tau_{12}}{T_{rs}}\right)^2\geq 1$	

X_C, Y_C, and Z_C—Axial and transverse compressive strength of a tow

T_L and T_T—Longitudinal and transverse shear strength of a tow

T_{rs}—Shear strength of a resin pocket

Note that the delamination criterion given in Table 1 is used to predict the microcracking induced debonding of a woven fabric unit cell (*x*-tow/*y*-tow/resin pocket). Since the micro-debonding failure occurs in a resin-rich zone, the stress components in the resin phase are used in the debonding failure criterion.

A set of internal damage variables (ω_i) are used to characterize the damage evolution and the resulting stiffness degradation based on the predicted failure mode listed in Table 1. A damage evolution algorithm for an anisotropic material developed by Matzenmiller et al. [24] is employed for the diffuse in-plane damage progression analysis. Given the damage thresholds r_i, (i=1, 2, ...11) associated with the ith failure criterion listed in Table 1, the corresponding damage variable ω_i can be determined by

$$\omega_i = 1 - e^{\frac{1}{me}\left(1-r_i^m\right)} \text{(no sum on index i)} \tag{14}$$

where m is a strain rate softening constant. Using Eq. (14), the stiffness reduction can be characterized by $C_i=(1-\omega_i)C_{i0}$, where C_{i0} is the stiffness at its virgin state.

Bridging model between the damaged plies and the resulting laminated plate

The progressive failure analysis of a large laminated composite ship structure is computationally intensive. Because of the non-uniform stress and damage distribution in the through the thickness direction, multiple layers of elements are needed to be introduced in the finite element model. While the use of the layered shell or layered solid elements can greatly enhance the computational efficiency, its modeling fidelity highly relies on the accuracy in determining the smeared laminated plate properties from the individual damaged ply properties. To construct the smeared laminated plate properties from its ply properties, the CELLMAT solver has to be integrated with a general purpose laminator (see Fig. 1).

Because of the non-uniform damage distribution in the through the thickness direction, the damaged laminated plate is no longer symmetric despite its initial symmetric configuration. The presence of larger transverse shear deformation will render the classical lamination theory inaccurate. In this study, a Reissner–Mindlin based lamination model (VAPAS) is selected as our laminator. VAPAS is developed by Yu [25, 26] based on the variational-asymptotic method to provide a generalized 2D constitutive law and accurate 3D recovery relations of a laminated composite plate/shell. The variational asymptotic method is employed to reduce the dimensionality systematically in terms of the smallness of h/l and h/R, where $h$is the thickness, l the characteristic wavelength of in-plane deformations, R the characteristic radius of curvatures for the undeformed reference surfaces. VAPAS decouples the nonlinear 3D problem into a linear, 1D, through-the-thickness analysis and a non-linear, 2D, plate/shell analysis. VAPAS implements the through-the-thickness analysis to calculate a generalized constitutive model for the 2D plate/shell analysis and recover the 3D distributions of displacements, strains and stresses based on the global responses. Validation studies have been performed in Ref. [25, 26] by comparing VAPAS predictions against the solutions from the classical lamination theory (CLT), the first-order shear-deformation theory (FOSDT), and 3D exact solution.

Cohesive interface model for delamination initiation and propagation

A multi-scale computational framework for characterizing continuum in-plane damage has been formulated in Sections ''Micromechanics cell model for an unbalanced plain weave'', ''Mechanism-driven failure criteria and continuum damage progression'', ''Bridging model between the damaged plies and the resulting laminated plate''. Due to the coexistence of continuum in-plane damage and discrete out-of-plane delamination damage, a cohesive interface model is implemented in the hybrid failure prediction tool via a user-defined material model in LS-DYNA3D. In the cohesive interface model, the traction force acting on the surface of a delamination crack is determined from the corresponding component of the displacement jump. For the demonstration purpose, an elastic cohesive model based on Tvergaard–Hutchinson (TH) [27] is employed in the current study.

To establish a mapping relation between fracture mechanics and the cohesive interface model, a pair of double nodes associated with the cohesive interface element is introduced where the top and the bottom node is defined as the slave and master node. A constitutive material model is introduced to compute the cohesive force based on the relative displacement between the slave and the master node. A cohesive law is formed to ensure that the crack absorbs the correct energy G_{iC} and that it can only propagate if sufficient stored energy is available from the surrounding material to drive crack growth. Based on the Tvergaard-Hutchinson (TH) model, the potential density ϕ from a given crack opening displacement Δu is defined by:

$$\phi(\Delta u) = \begin{cases} \sigma_{\max}\frac{\lambda}{\lambda_1}; & \lambda<\lambda_1 \\ \sigma_{\max}; & \lambda_1\leqslant\lambda\leqslant\lambda_2 \\ \sigma_{\max}\frac{1-\lambda}{1-\lambda_2}; & \lambda_2<\lambda\leqslant 1.0 \\ 0.0; & \lambda>1.0 \end{cases}. \tag{15}$$

The potential Φ can be obtained from the potential density via

$$\Phi = \delta_n \int_o^{\lambda} \phi(\eta)\mathrm{d}\eta, \tag{16}$$

and the traction can be calculated from the potential Φ by

$$T_i = \frac{\partial \Phi}{\partial \Delta u_i}. \tag{17}$$

In Equation (15), $\sigma_{\max}$ is the maximum cohesive force and λ is the dimensionless total crack opening displacement defined by:

$$\lambda = \sqrt{\left[\left(\frac{\Delta u_1}{\delta_t}\right)^2 + \left(\frac{\Delta u_2}{\delta_t}\right)^2 + \left(\frac{\Delta u_3}{\delta_n}\right)^2\right]}, \tag{18}$$

where δ_t and δ_n is the critical crack opening displacement in Mode II (Mode III) and Model I, respectively. The parameters λ_1 and λ_2 in Eq. (15) denote the dimensionless crack opening displacement at the initial peak traction and the final peak traction, respectively. By substituting Eqs. (15) and (16) into Eq. (17), the tangential crack surface traction (T_i; i=1, 2) can be determined by:

$$T_i = \begin{cases} \left(\sigma^i_{\max}/\lambda_1\right)(\Delta u_i/\delta_t)(\delta_n/\delta_t); & \lambda < \lambda_1 \\ \left(\sigma^i_{\max}/\lambda\right)(\Delta u_i/\delta_t)(\delta_n/\delta_t); & \lambda_1\leqslant\lambda\leqslant\lambda_2 \\ \left(\sigma^i_{\max}/(1-\lambda_2)\right)((1-\lambda)/\lambda)(\Delta u_i/\delta_t)(\delta_n/\delta_t); & \lambda_2 < \lambda\leqslant 1.0 \\ 0.0; & \lambda > 1.0 \end{cases}. \tag{19}$$

The normal traction force associated with Mode I fracture is computed by:

$$T_n = \begin{cases} \left(\sigma^n_{\max}/\lambda_1\right)(\Delta u_3/\delta_n); & \lambda < \lambda_1 \\ \left(\sigma^n_{\max}/\lambda\right)(\Delta u_3/\delta_n); & \lambda_1\leqslant\lambda\leqslant\lambda_2 \\ \left(\sigma^n_{\max}/(1-\lambda_2)\right)((1-\lambda)/\lambda)(\Delta u_3/\delta_n); & \lambda_2 < \lambda\leqslant 1.0 \\ 0.0; & \lambda > 1.0 \end{cases}. \tag{20}$$

During numerical implementation of the above cohesive interface model, the crack opening displacement (Δu_i) defined in Eqs. (19) and (20) is computed from the relative nodal displacement and then transformed to the local crack coordinate system with z along the normal direction of the crack surface. In addition, the model is numerically implemented using a dimensionless

displacement jump. Thus, the critical crack opening displacement (λ_C) has a constant value of 1.0 in its dimensionless space.

The original TH-model is developed based on a trapezoidal shape function for both the tangential traction (T_i) in Eq. (19) and the normal traction (T_n) in Eq. (20). For the current 3D fracture problem, it is assumed that both the critical crack opening displacement and the maximum cohesive force under Mode II and Mode III are the same. Thus, the energy release rate associated with the normal (Mode I) and tangential (Mode II or Mode III) mode can be computed by:

$$G_{\mathrm{I}} = \int_0^{\delta_n} T_n \mathrm{d}\delta \quad G_{\mathrm{II}} = \int_0^{\delta_t} T_t \mathrm{d}\delta. \tag{21}$$

Given the trapezoidal function for the cohesive force, $T(\lambda)$, the critical crack opening displacement (δ_n,δ_t) can be determined from the following energy balance equation by:

$$G_{\mathrm{IC}} = \frac{1}{2}\sigma^n_{\max}\delta_n(1-\lambda_1+\lambda_2) \quad G_{\mathrm{IIC}} = \frac{1}{2}\sigma^t_{\max}\delta_t(1-\lambda_1+\lambda_2). \tag{22}$$

There are six parameters associated with the general TH-model. They are: (1) the maximum normal cohesive force ($\sigma^n{}_{\max}$); (2) the maximum tangential cohesive force ($\sigma^t{}_{\max}$); (3) the critical normal crack opening displacement (δ_n); (4) the critical tangential crack opening displacement (δ_t); (5) the shape factor λ_1; and (6) the shape factor λ_2. For the triangular cohesive model, we can simply assume $\lambda_1 = \lambda_2 = \lambda$, where λ can be determined from the ratio of the crack opening displacement at initiation and propagation by $\lambda = \delta_0/\delta_C$.

Summary of solution procedure in hybrid damage prediction tool

To capture the constituent driven continuum failure progression and the synergistic interaction between the discrete and continuum damage, a hybrid progressive damage model is developed and integrated with the LS-DYNA3D finite element solver. Both the continuum damage model and the cohesive interface model are implemented in LS-DYNA3D via the user-defined material models. To prevent the penetration of the upper and lower cracked surface under compressive loading, an eroding single surface contact is applied during the numerical solution process. The key solution procedure is summarized below

- characterization of composite ply properties from its constituent properties at a given damage state via CELLMAT;
- propagation of individual damaged ply properties into the VAPAS laminator for quantification of composite properties at the laminate level;
- performance of a FEM based structural response analysis using the LS-DYNA3D FEM solver;
- decomposition of composite stress/strain response into its constituent stress/strain at a Gaussian point via CELLMAT;
- application of a constituent based failure criterion for a rational stiffness degradation based on the predicted failure mode;
- generation of new composite properties for next loading stage;
- characterization of delamination failure at the interface via a cohesive element model;
- quantification of interface delamination at each loading stage in the presence of surrounding continuum damage.

Both the applicability and accuracy of the hybrid dynamic failure prediction tool are demonstrated next via its application to a sub-structural component subjected to dynamic shock and impact loading.

Example applications of the hybrid dynamic failure prediction tool

To demonstrate the applicability of the developed hybrid dynamic failure prediction tool, three examples are presented here: (1) a circular plate subjected to a shock loading; (2) a composite hat stiffener under a low velocity impact; and (3) a composite sandwich beam subjected to a drop weight impact. Dynamic tests have been performed on structural components associated with Example 1 and Example 2 to (i) understand the dynamic response and failure mechanisms; (ii) determine the ability of current analytical tools for response and damage prediction; and (iii) use the test data to evaluate the fidelity of the state-of-the-art composite material damage models. The goal from this combined experimental and analytical study is to reduce the high cost and time associated with a test-driven shock certification. Example 3 is used to demonstrate the synergistic interaction between the in-plane continuum damage and the out-of-plane discrete damage (delamination).

A circular woven fabric laminated plate subjected to dynamic pressure loading

The circular composite panel specimen fabricated by Seemann Composites, Inc. uses the 24 ounce woven roving E-glass balanced weave with the vinyl ester resin. The overall fiber volume fraction in the plain weave is 51%.

The laminated plate has 16 plies with the thickness of 9.652 mm (0.38 in). Given the elastic properties for each constituent shown in Table 2, the effective ply properties predicted from CELLMAT are summarized in Table 3. The lamination sequence of the plate is $[0/45/90/-45]_{2s}$ with the ply thickness of 0.60325 mm. As shown in Fig. 5, the plate of radius of 0.114 m (4.5 in) is mounted between the steel mounting flange and the steel retaining ring. Figure 6 shows a list of elements where the strain gauges are placed. The bottom surface of the laminated plate is hit by a shock wave generated from a given dynamic impact.

Using the ply properties given in Table 3 and the stacking sequence of $[0/45/90/-45]_{2s}$, the 16-ply laminated plate properties are computed from the VAPAS laminator [25–26]. The smeared solid elastic constants of the laminate at its virgin state are given in Table 4. Given the applied boundary conditions, the dynamic pressure generated from a shock loading on the bottom surface is not uniform. A comparison of time histories of dynamic pressures at the selected elements at bottom is given in Fig. 7. For the progressive failure analysis, the in-situ constituent strength parameters are derived from the unidirectional composite model and given in Table 5.

Table 2 Summary of constituent properties of seemann composite (plain weave)

Thermal/mechanical properties	E-glass (Fiber)	Vinyl ester (Matrix)
Elastic modulus E (psi)	1.05×10^7	4.71×10^5
E (GPa)	72.45	3.25
Poisson's ratio v	0.225	0.325
Coefficient of thermal expansion $\kappa(\mu\varepsilon/K)$	5.4	65

Table 3 Summary of orthotropic ply properties at its virgin state generated from CELLMAT

Ply-orthotropic material properties	CELLMAT-prediction
E_x (psi)	3.599×10^6
E_x (GPa)	24.82
E_y (psi)	3.599×10^6
E_y (GPa)	24.82
E_z (psi)	1.567×10^6
E_z (GPa)	10.80
v_{xy}	0.1387
v_{xz}	0.3163
v_{yz}	0.3163
G_{xy} (psi)	0.652×10^6
G_{xy} (GPa)	4.496
G_{xz} (psi)	0.4888×10^6
G_{xz} (GPa)	3.370
G_{yz} (psi)	0.4888×10^6
G_{yz} (GPa)	3.370

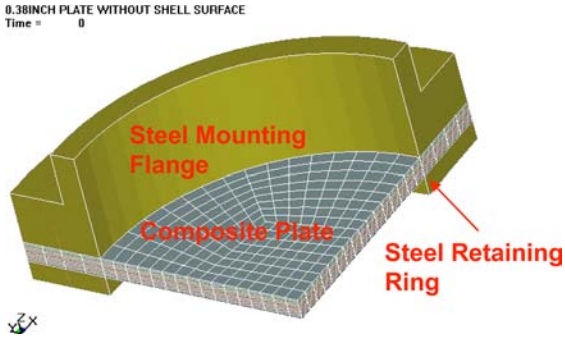

Fig. 5 A circular laminated composite plate subjected to a dynamic shock wave on the bottom surface

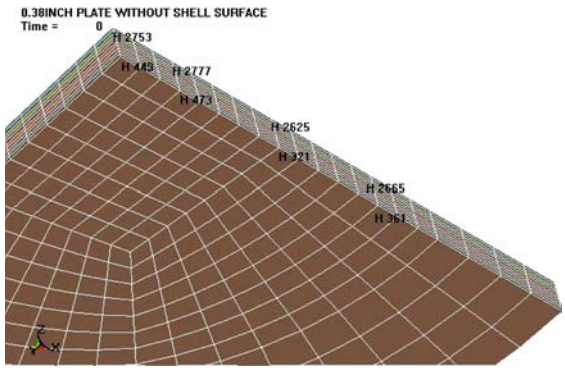

Fig. 6 List of locations of strain gauges on the top and bottom of the plate

Table 4 Summary of undamaged laminated plate properties

Laminate-orthotropic material properties	VAPAS-prediction
E_x (psi)	2.910×10^6
E_x (GPa)	20.06
E_y (psi)	2.910×10^6
E_y (GPa)	20.06
E_z (psi)	1.568×10^6
E_z (GPa)	10.81
v_{yx}	0.3036
v_{zx}	0.1377
v_{zy}	0.1377
G_{xy} (psi)	1.116×10^6
G_{xy} (GPa)	7.695
G_{xz} (psi)	0.4888×10^6
G_{xz} (GPa)	3.370
G_{yz} (psi)	0.4888×10^6
G_{yz} (GPa)	3.370

To demonstrate the accuracy and validity of the continuum damage model for progressive failure prediction, the strain gauge data measured from multiple tests are used to compare with the strain response prediction at a given location. A comparison of time histories of strain prediction at element 2665 and 361 near the clamped edge (see Fig. 6) is shown in Fig. 8, and 9, respectively. While the peak strain response from the model prediction is slightly

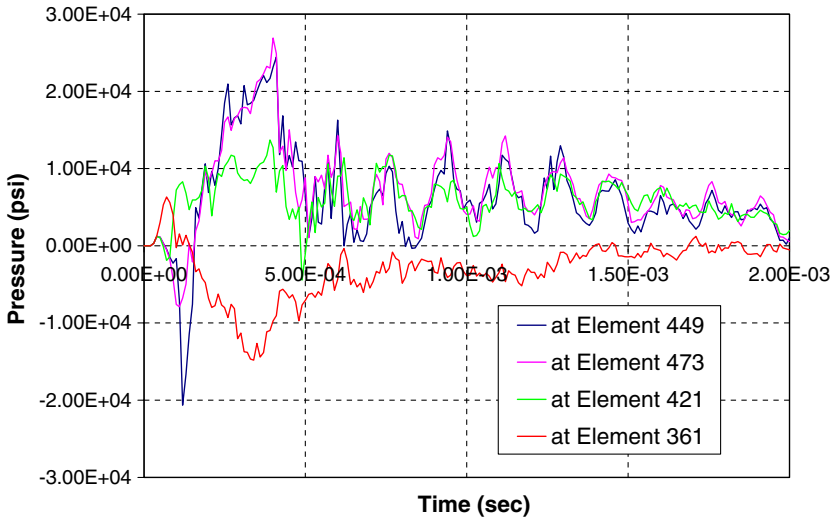

Fig. 7 Comparison of time histories of applied pressure at selected elements of bottom plate shown in Fig. 6

Table 5 Summary of constituent strength parameters used in the user-defined material model in LS-DYNA3D

Strength parameters	Numerical value used in continuum damage model
X_T (ksi/MPa)	48.4/333.72
X_C (ksi/MPa)	42.2/290.97
Y_T (ksi/MPa)	43.6/300.62
Y_C (ksi/MPa)	38.7/266.84
Z_T (ksi/MPa)	7.8/53.78
Z_C (ksi/MPa)	60.0/413.70
T_L (ksi/MPa)	7.4/51.02
T_T (ksi/MPa)	7.4/51.02
T_{rs}(ksi/MPa)	7.4/51.02

lower than the test data, the general trend from the model prediction agrees well with the experimental observation. The lower predictions for the maximum strain response are attributed to the effect from the lower strain predictions at the Gaussian points which are not exactly at the gauge locations on the surface. To further demonstrate the accuracy of the constituent based failure prediction using the mechanism-driven failure criteria given in Table 1, a comparison of predicted microcracking-induced debonding zone (interlaminar failure) is shown in Fig. 10. The size of the predicted damage zone matches well with the experimental observation.

In order to examine the effects of the plate thickness on the final damage distribution, two different types of specimens with the plate thickness of 0.58″ (14.7 mm) and 0.86″ (21.8 mm) are used in the shock tests. The predicted damage patterns for the top and bottom side of the 0.58″, and 0.86″ specimens are shown in Fig. 11 and 12. In these Figures, the spatial distribution of the accumulative damage parameter associated with the inter-ply debonding (ω_d) is plotted with the red region

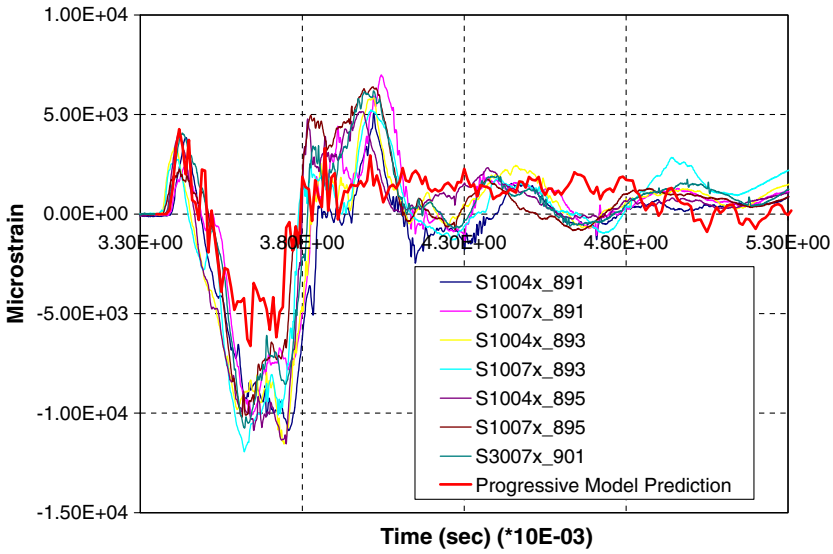

Fig. 8 Comparison of strain response prediction at element 2665 with strain gauge data

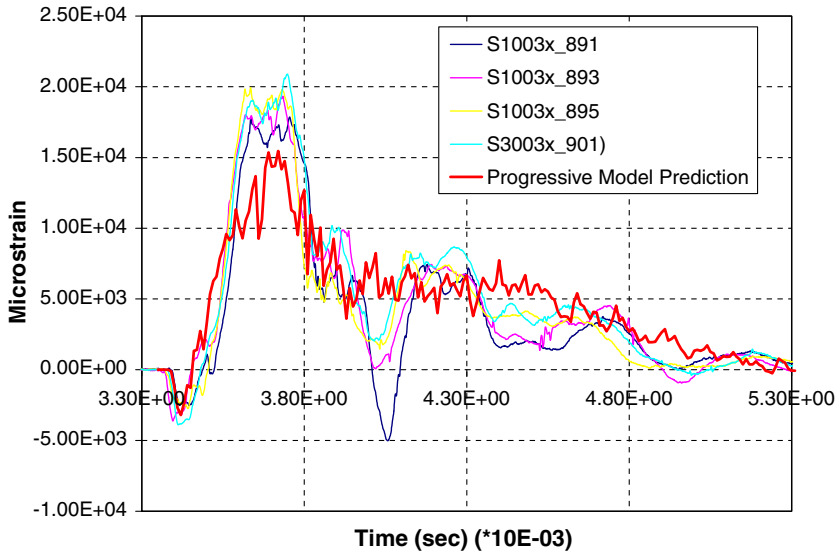

Fig. 9 Comparison of strain response prediction at element 361 with strain gauge data

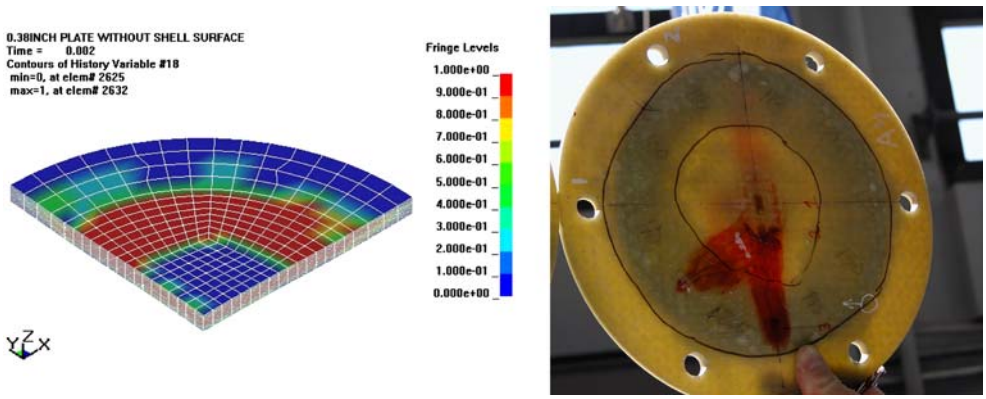

Fig. 10 Comparison of predicted damage with experimental observation

indicating the complete microcracking-induced debonding failure ($\omega_d = 1$) and the blue region representing $\omega_d = 0$. The light blue and green colors indicate the partial damages associated with the matrix cracking in the resin pocket and in the X- or the Y-tow. While the size of the inter-ply damage zone is reduced significantly with the increase of the plate thickness, an interior matrix cracking zone is still shown in Fig. 12. In addition, a small debonding zone can be seen also on bottom of the 0.86″ specimen. For the thickest plate (0.86″), it can be expected that both the matrix cracking and debonding failure are initiated mainly due to the higher transverse shear stress.

A composite hat stiffener subjected to low velocity impact at the baseplate

After demonstrating the validity of the continuum damage model, a composite hat stiffener subjected to a low velocity impact is considered to demonstrate the applicability of the cohesive interface model described in Section ''Cohesive interface model for delamination initiation and propagation''. The composite hat stiffener is mounted on a shock table that is impacted by a hammer at a given drop height. The test set-up and instrumentation are used to study the failure mode and failure energy of a bonded structure at a sub-scale level.

To reduce the computational effort, a half-symmetry solid model shown in Fig. 13 is used for the low velocity impact analysis. A cap mass of same weigh and dimension as in the test setup is incorporated in the model analysis. Given the measured time history of the shock table motion after an impact, a prescribed displacement boundary condition is defined at the location of the half rounds clamper. As shown in Fig. 13, the hat stiffener consists of (1) E-glass/vinyl ester woven fabric laminated plate (baseplate); (2) web stiffener reinforcement (upper/side/lower/taper); (3) syntactic foam; and (4) structural putty. In this

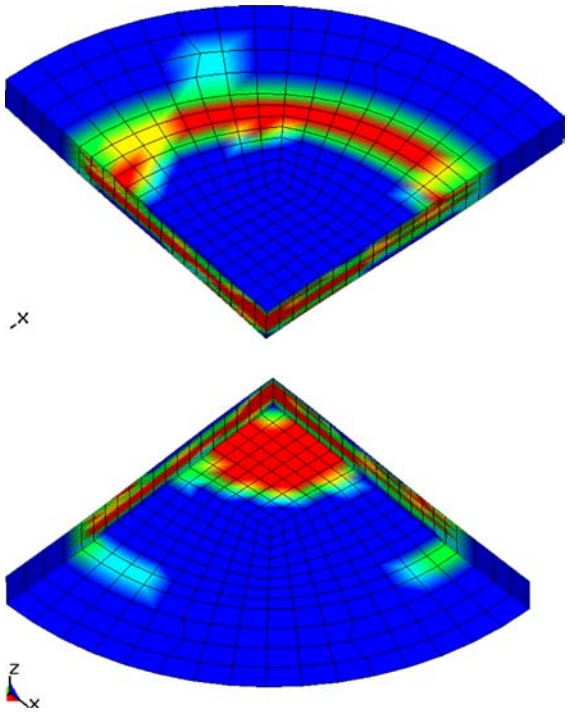

Fig. 11 Display of inter-ply damage zone predicted by the continuum damage module in 0.58″ thick specimen

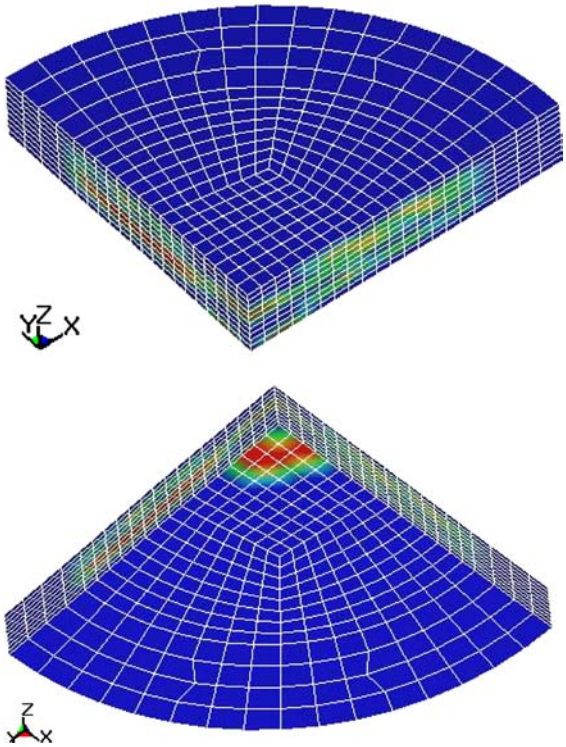

Fig. 12 Display of inter-ply damage zone predicted by the continuum damage module in 0.86″ thick specimen

example problem, the critical values of the strain energy release rate are collected from the ARL Report [28]. The Mode I and Mode II G-values are given by

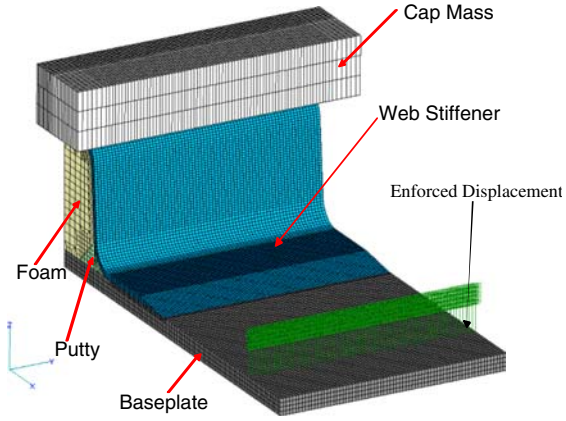

Fig. 13 Half-symmetry solid model of a composite hat stiffener

$$G_{\mathrm{Ic}} = 2.653\,\mathrm{in} - \mathrm{lb/in}^2 \quad G_{\mathrm{IIc}} = 6.256\,\mathrm{in} - \mathrm{lb/in}^2. \tag{23}$$

Based on the experimental calibration, the maximum cohesive strength associated with Model I and Model II/III are given by

$$\sigma^n_{\max} = 1644.22\mathrm{psi} \quad \sigma^t_{\max} = 2516.44\mathrm{psi}. \tag{24}$$

Substituting Eqs. (23) and (24) into Eq. (22) and using λ_1=λ_2, the critical crack opening displacements for normal mode (Model I) and shear mode (Mode II or Mode III) are given by:

$$\delta_n = 3.227 \times 10^{-3}\,\mathrm{in} \quad \delta_t = 4.972 \times 10^{-3}\,\mathrm{in}. \tag{25}$$

Given the composite material properties (same as in Example 1), cohesive model parameters (Eqs. (23)–(25)), and the initial impact condition, the progression of damage predicted from the cohesive model is shown in Fig. 14 from crack initiation, propagation, to the final separation. As shown in Fig. 14, a crack is initiated at the tip of the putty from its outer edge. Visible crack initiation is predicted here at 41.6 ms; approximately 0.8 ms after experimentally observed initiation. The crack then propagates in both directions, with faster growth toward the web taper. Because of the intensified stress field at the tip of the web taper, a second crack is initiated in the vicinity of the tip of the web taper from its corner. Coalescence of the 1st and the 2nd cracks results in complete debonding between the web taper and the base plate. Finally, the coalesced crack propagates towards the foam, resulting in complete unzipping along the interface. The failure sequence and failure patterns shown in Fig. 14 agree well with the experimental observations from a high speed camera as shown in Fig. 15.

Because of the intensified shear cohesive force zone at the outside edge of the putty tip (see the blue color zone in Fig. 16), a crack will be initiated there due to the

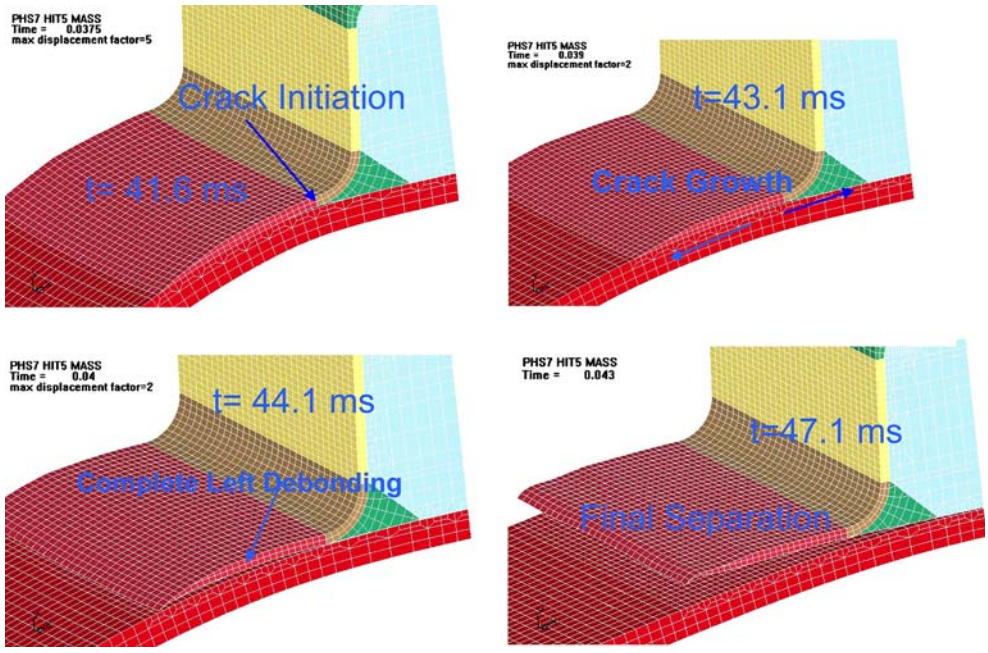

Fig. 14 Predicted delamination damage progression along the interface of the hat stiffener

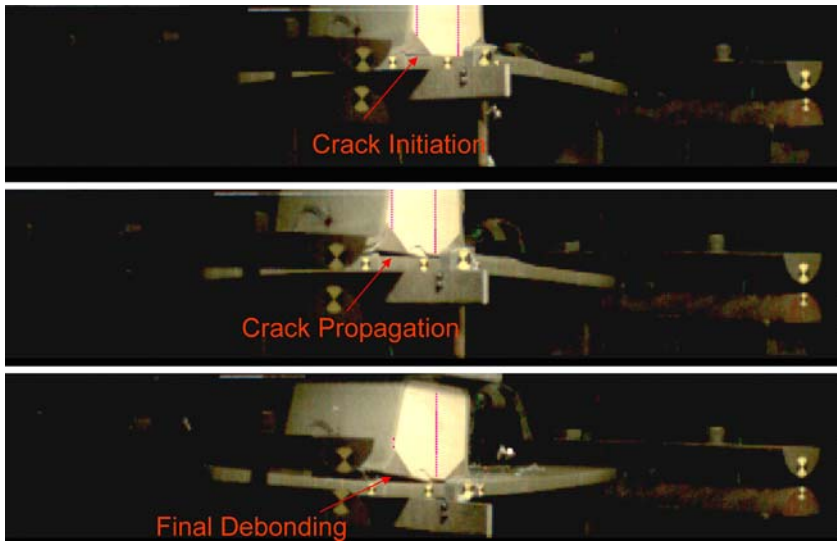

Fig. 15 Illustration of failure events observed from a high speed camera

deletion of the cohesive element. To illustrate the crack growth pattern along with the time evolution of the cohesive shear stress, the damage progression of the cohesive patch is shown in Fig. 16 along with the distribution of the cohesive shear force. As shown in Fig. 16, the crack growth pattern is nearly symmetric with respect to the global *xy*-plane. A Model II crack is initiated at the tip of the putty from its outside edge. After initiation, the crack propagates in the horizontal (x) and the through-the-thickness (z) direction. A second crack is then initiated at the corner of the web taper and propagates in both the x- and z-directions. Finally, debonding between the foam core and the base plate occurs resulting in a complete separation. Both the failure sequence and the time of delamination initiation agree well with the experimental observations.

A sandwich beam subjected to a low velocity impact

The accuracy of the continuum damage and the discrete damage prediction module within the hybrid damage prediction tool has been demonstrated via its application in Example 1 (see Section ''A circular woven fabric laminated plate subjected to dynamic pressure loading'') and 2 (Section ''A composite hat stiffener subjected to low velocity impact at the baseplate''), respectively. To explore

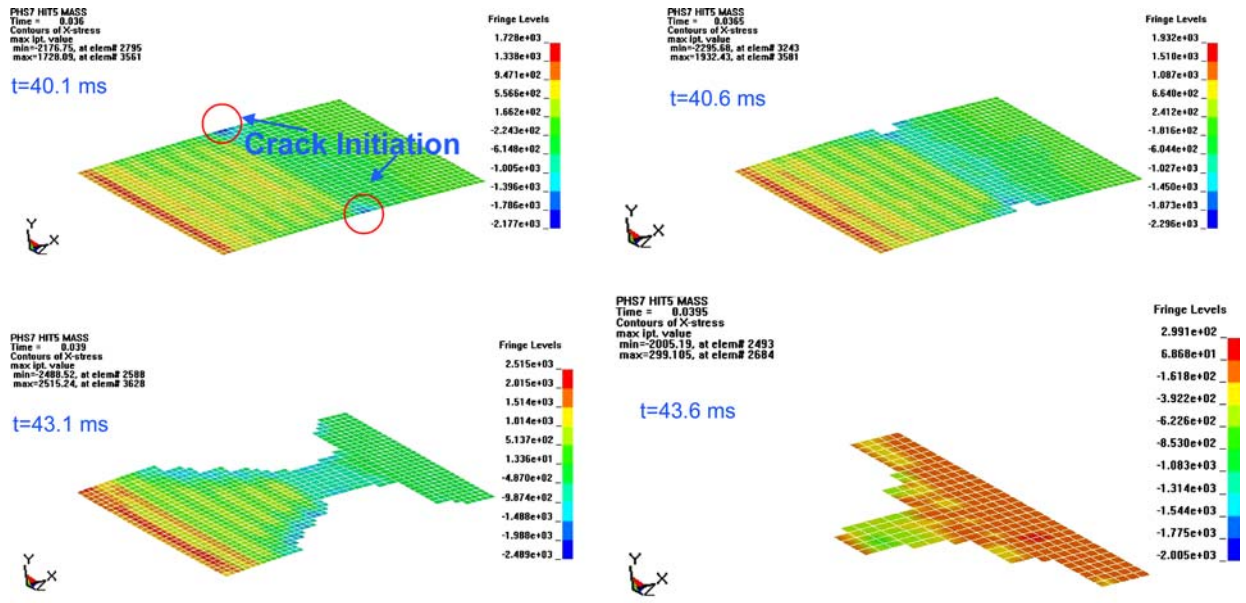

Fig. 16 Illustration of crack growth pattern and time evolution of cohesive shear force

the compounding effects from the coexistence of the continuum and discrete damage, a sandwich beam subjected to a low velocity impact is considered here. The top and bottom skin thickness of the sandwich beam is 0.7″ (17.78 mm) while the thickness of the middle core layer is 3.5″ (88.9 mm). Three (3) elements are used to discretize both the top and bottom skin layer made of E-glass/vinyl ester plain weave laminated plate. The material properties of the skin are the same as those used in Example 1. The Balsa core layer is discretized into five (5) elements and its material and strength parameters are listed in Table 6 and 7, respectively.

The length (L), width (W), and height (H) of the sandwich beam are given by 100″ (2.54 m), 10″ (0.254 m), and 4.9″ (0.124 m), respectively. The resulting finite element model has 5,978 nodes and 4,689 elements. As shown in Fig. 17, the beam is clamped at both end and an impulsive pressure load is applied at the center of the beam. The time history of the pressure load $P(t)$ shown in Fig. 18 is associated with a drop weight impact test with the peak pressure of 120 *psi*. In order to simulate the delamination failure in addition to the continuum damage in the sand-

Table 6 Summary of undamaged Balsa core properties

Laminate-orthotropic material properties	VAPAS-prediction
E_x (psi)	2.175×10^4
E_x (MPa)	150.0
E_y (psi)	2.175×10^4
E_y (MPa)	150.0
E_z (psi)	5.801×10^5
E_z (GPa)	4.0
v_{yx}	0.499
v_{zx}	0.333
v_{zy}	0.333
G_{xy} (psi)	7.252×10^3
$G_{xy}(MPa)$	50.0
G_{xz} (psi)	2.321×10^4
G_{xz} (MPa)	160.0
G_{yz} (psi)	2.321×10^4
G_{yz} (MPa)	160.0

Table 7 Summary of strength parameters of the Balsa Core

Strength parameters	Numerical value used in continuum damage model
X_T (ksi/MPa)	1.088/7.501
X_C (ksi/MPa)	0.928/6.398
Y_T (ksi/MPa)	1.088/7.501
Y_C (ksi/MPa)	0.928/6.398
Z_T (ksi/MPa)	1.958/13.50
Z_C (ksi/MPa)	1.842/12.70
T_L (ksi/MPa)	0.435/3.0
T_T (ksi/MPa)	0.435/3.0
T_{rs} (ksi/MPa)	0.435/3.0

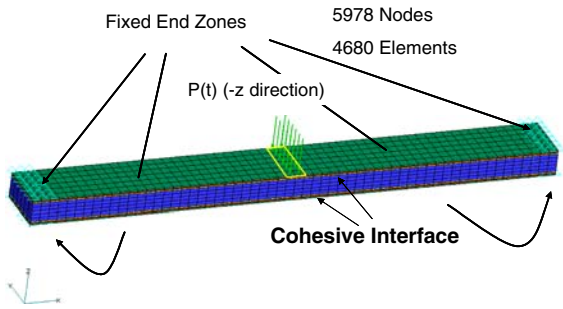

Fig. 17 A FEM Model of a sandwich beam subjected to a drop weight test

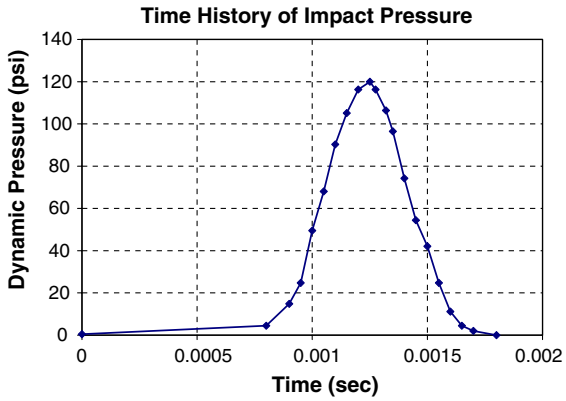

Fig. 18 Time history of pressure load resulted from a drop weight impact

wich beam, two cohesive interface layers are introduced between the top/bottom skin and the core material. The cohesive material parameters are assumed as the same as those in Example 2. The developed computational hybrid tool is used to simulate the response and damage progression in this three point bending specimen subjected to a drop weight impact loading.

The damage is initiated via the delamination between the top skin and core layer at t = 1.23 ms. The delamination is driven dominantly by Model I and the distribution of the normal cohesive force before and after the delamination crack initiation is shown in Fig. 19. As shown in Fig. 19, the intensified normal cohesive stress (σ_{zz}) at the center edge of the top skin/core interface gives rise to the edge crack initiation. To further examine the event of delamination initiation, the time history of σ_{zz} at a failed interface element is shown in Figure 19. Once σ_{zz} achieves its critical value of 1,644.22 psi (see Eq. (24)), a sudden drop in σ_{zz} indicates the initiation of a delamination crack. After the crack initiation at its outside edge, it propagates toward the center to from a through-the-width crack.

After forming the through-the-width delamination crack at t = 1.26 ms, the compressive bending stress at the top skin is released and additional stress will be exerted on the core resulting in matrix cracking. There is no core damage before the delamination initiation. Because of the synergistic damage interaction, both the initiation and propagation of the delamination crack will accelerate the core damage as shown in Fig. 20. In Fig. 20, two through-the-thickness core microcracking zones are formed near both tips of an interface delamination crack. The final damage pattern resulted from the discrete and continuum damage interaction is shown in Fig. 21. The delamination crack between the top skin and the core propagates in both direction and the final delamination crack is spanned over four skin element length as shown in Fig. 21. An intensified microcracking zone directly beneath the delamination crack is formed in the middle of the core layer. The microcracking is extended more horizontally in the core along both the top and bottom skin/core interface resulting in an H-shaped damage pattern as shown in Fig. 21.

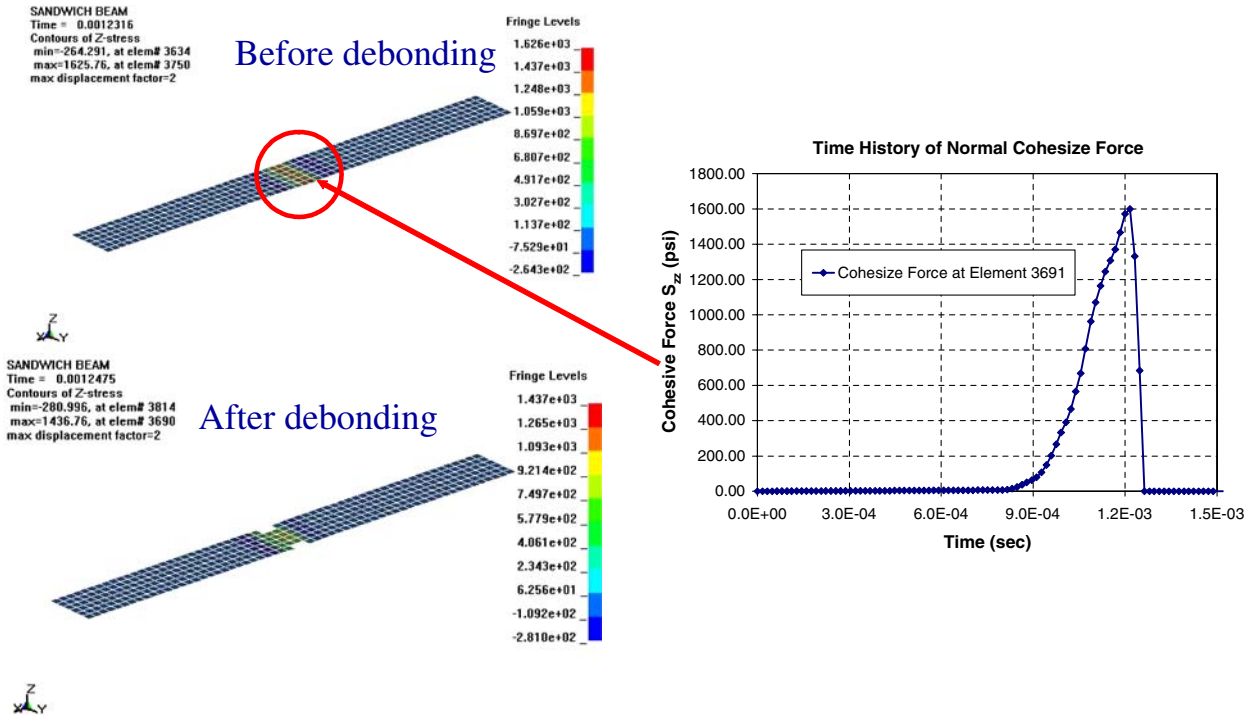

Fig. 19 Display of delamination initiation and model I cohesive stress distribution before and after the failure initiation

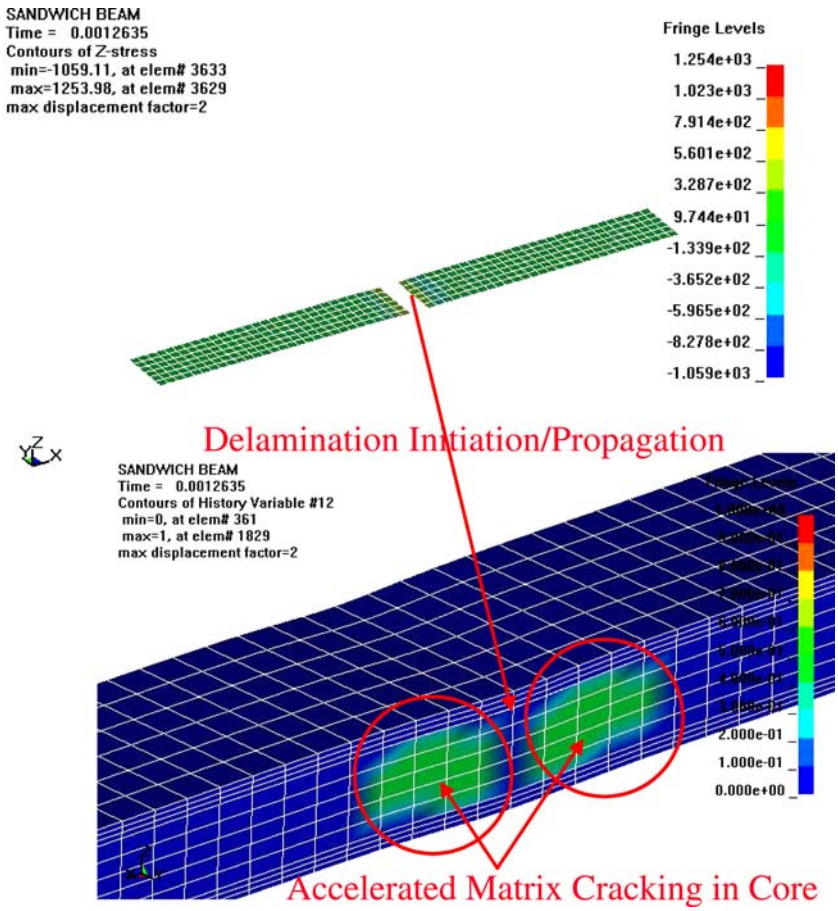

Fig. 20 Illustration of accelerated matrix cracking in core due to the initiation of delamination

Conclusions

A hybrid dynamic failure prediction tool has been developed to capture the synergistic interaction between the continuum and discrete damage. The tool has been implemented in LS-DYNA3D environment via a user-defined material model. A multi-scale solution framework is formulated to determine the material response and failure at the structural level from its constituent, ply, and laminated plate level. A dual-function micromechanics model (CELLMAT) is developed for an unbalanced weave subjected to a thermal–mechanical load. The developed micromechanics model can not only characterize the effective thermal–mechanical properties of the unbalanced weave for given constituent damage, but can also compute the stress and strain at each constituent. The calculated constituent stress and strain has been used in a mechanism-driven failure criterion. The integration of the dual-function micromechanics model with a constituent-based failure criterion provides an additional window to reveal the failure mode and failure sequence during a progressive failure analysis.

To further enhance the computational efficiency, the CELLMAT solver has been integrated with the VAPAS laminator. The integration of CELLMAT and VAPAS provides an efficient and accurate material translator for a commercial finite element solver in (1) computing the smeared element properties from a given constituent damage; and (2) determining the constituent response parameters for the mechanism-driven failure prediction and the subsequent material degradation. The physical mapping established among these different length scales will provide a rational way to explore an optimal material and processing procedure for a given design requirement of a composite ship structure.

To accurately capture the non-self-similar delamination crack growth, a cohesive interface model has been developed and linked with the LS-DYNA3D via a user-defined material model. Because of its continuum damage mechanics nature, it can be easily integrated with the diffuse in-plane continuum damage model. The resulting hybrid damage prediction tool can effectively study the coupling effects between the in-plane and the out-of-plane failure modes in composite structures, such as composite joints or sandwich structures.

The applicability and accuracy of the hybrid dynamic failure prediction have been demonstrated via its application to (1) a circular plate subjected to a shock wave loading; (2) a composite hat stiffener subjected to a low

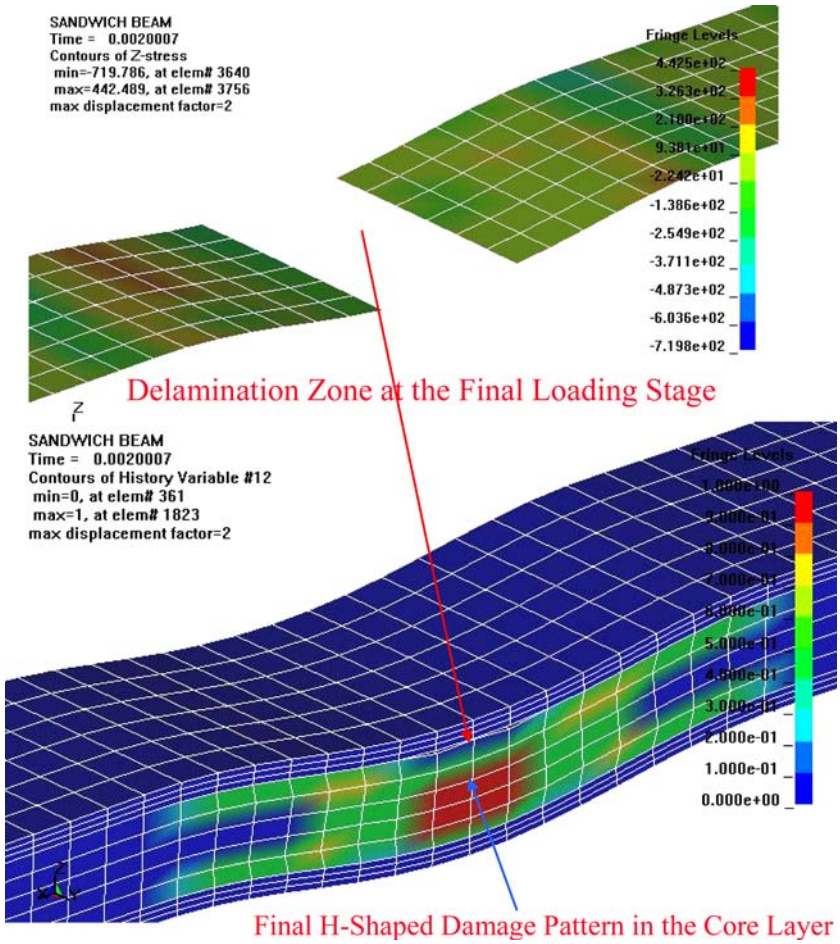

Fig. 21 Illustration of discrete and continuum damage interaction and the resulting damage pattern at the final loading stage

velocity impact; and (3) a sandwich beam subjected to a drop weight impact. The time histories of strain data measured from the circular plate agree well with the constituent based damage prediction. The predicted failure events associated with the progression of a disbonding crack also agree well with the experimental observations. The core damage process accelerated from the interface crack initiation and propagation is explored via the tool application to the sandwich beam subjected to a low velocity impact. With the validated dynamic failure prediction tool coupled with the standardized sub-scale dynamic tests, a cost-effective certification procedure can be established for critical composite ship structures subjected to an aggressive loading environment.

Acknowledgments The support of Navy Labs and the Office of Naval Research, Code 331, is gratefully acknowledged.

References

1. Yang Q, Cox B (2005) Intl J Fract 133:107
2. Lua J, Key C, Schumacher SC, Hansen A (2004) Shock Vibrat 11(2):103
3. Iannucci L (2006) Int J Impact Eng, 32(6):1013
4. Williams KV, Vaziri R (2001) Comput Struct 79:997
5. Lee Y, Huang C-H (2003) J Reinforced Plastics Comp 22:1059
6. Yen CF (2002) In: Proceeding of the 7th International LS-DYNA Users Conference, Dearborn, MI, May 19–21
7. Key C, Lua J (2006) Comp Part A 37(7):1005
8. Bahei-El_Din YA, Rajendran AM, Zikry MA (2004) Int J Solids Struct 41:2307
9. Zako M, Uetsuji Y, Kurashiki T (2003) Finite element analysis of damaged woven fabric composite materials, Comp Sci Tech 63:507
10. Tabiei A, Ivanov I (2004) Int J Non-Linear Mech 39:174
11. Key CT, Six RW, Hansen AC (2003) Comp Sci Technol 63(13):1857
12. Alfano G, Crisfield MA (2001) Finite element interface models for the delamination analysis of laminated composites: mechanical and computational issues. Intl J Numer Methods Eng 50:1701
13. Borst RD, Remmers JJC, Needleman A (2006) Mesh-independent discrete numerical representations of cohesive-zone models. Eng Fract Mech 73:160
14. Krueger R (2002) The virtual crack closure technique: history, approach and applications; NASA/CR-2002-211628
15. Xie D, Chung J, Waas AM, Shahwan KW, Schroeder JA, Boeman RG, Kung V, Klett LB (2005) Intl J Fract 134:231
16. Lua J, O'Brien J (2003) In: Proceeding of Composites in Fire 3, Sept. 9–10, 2003, Newcastle upon Tyne, UK
17. Lua J, Key CK, O'Brien J, Lopez-Anido RA, El-Chiti FW, Dagher H, Hess P (2004) In: Proceedings of the Joint American Society for composites/American Society For testing and materials committee D30. Oct. 17–20, 2004, Atlanta, GA

18. Lua J, O'Brien J, Key C, Wu Y, Lattimer B (2006) Comp Part A, 37(7):1024
19. Lua J (2006) Comp Part A (accepted for publication)
20. Tabiei A, Ivanov I (2004) Int J Non-Linear Mech 39:174
21. Hashin Z (1980) J Appl Mech 47:329
22. Tsai S, Wu E (1971) J Comp Mater 5:58
23. Paris F, A study of failure criteria of fibrous composite materials, NASA/CR-2001-210661, 2001; NASA Langley Research Center
24. Matzenmiller A, Lublinear J, Taylor RL (1995) Mech Mater 20:125
25. Yu W, Hodges DH, Volovoi VV (2002) Intl J Solids Struct 39(20):5185
26. Yu W (2005) Inl J Solids Struct, in press
27. Tvergaard V, Hutchinson JW (1992) J Mech Phys Solids 40:1377
28. Strauch EC, Strait LH (1999) Characterization of strain energy release rates for primary and secondary scrimp bondlines in composite panels. Technical Memorandum, Applied Research Laboratory, Penn State. State College, PA